Article

In Vitro Investigation of Gas Embolism in Microfluidic Networks Mimicking Microvasculature

Mohammad Mahdi Mardanpour[1,†], Ayyappasamy Sudalaiyadum Perumal[1,†], Zahra Mahmoodi[1], Karine Baassiri[1], Gala Montiel Rubies[1], Kenneth M. LeDez[2] and Dan V. Nicolau[1,*]

[1] Department of Bioengineering, Faculty of Engineering, McGill University, Montreal, Québec, H3A 0E9, Canada

[2] Faculty of Medicine, Memorial University, Health Sciences Centre, St. John's, Newfoundland and Labrador, A1C 5S7, Canada

[*] Correspondence: Dan V. Nicolau: dan.nicolau@mcgill.ca

[†] These authors contributed equally to this work.

Abstract: Gas embolism is a medical condition leading to the blockage of blood flow in the microvasculature by gas bubbles. While reported as rare, gas embolism often has devastating, fatal physiological consequences. Despite this acute importance, the genesis and evolution of air bubbles in blood vessels under different physiological conditions, such as blood viscosity and blood flow rate, is still understudied, largely because of difficult experimentation and in situ visualization. The objective of this work was to study the gas embolism phenomenon in vitro, using a microfluidic system that mimicked the architecture of microvasculature. The microfluidic systems comprised linear channels with two different air inlet types, namely, T- and Y-junctions with three different widths (20 µm, 40 µm, and 60 µm), and a 30 µm width honeycombed network with three bifurcation angles (30°, 60°, and 90°). Three synthetic liquids equivalent to 0%, 20%, and 46% hematocrit that mimicked the physiological blood viscosity and hematocrit concentrations were used. Our results show that: (i) 20 µm and 40 µm width channels had an elevated risk of gas embolism due to wide fluctuations in the total slug sizes; (ii) the resistance to the flow of air bubbles increased with the increase in the equivalent concentration of hematocrit; (iii) gas bubbles causing blockages and dampening of the flow velocity were frequently observed in 20 µm channels, and lastly (iv) increased risk of gas embolism was observed in the honeycomb architecture with 60° and 30° bifurcations. This work suggests that in vitro experimentation using microfluidic devices with microvascular tissue-like structures opens the possibility of studying this medical condition with high reproducibility and impacts the fact-based medical guidelines for preventing or mitigating iatrogenic occurrences.

Keywords: gas embolism; microfluidics; microvasculature; flow pattern

1. Introduction

Gas embolism is a medical condition consisting of the blockage of blood flow in the microvasculature by gas bubbles. While reported as rare, gas embolism has often devastating physiological consequences, including brain injury, disabilities, or even death.[1, 2] Gas emboli, sometimes entitled air embolism, can be introduced either endogenously or exogenously, leading to detrimental tensions in vascular endothelial cells. More dramatically, drastically reducing blood and oxygen supply to tissues, thus causing venous gas embolism (V.G.E.),[3-5] arterial blockages (arterial gas embolism, A.G.E.),[6] cerebral (cerebral gas embolism, C.G.E.)[7-10] and tissue ischemia.[11, 12] Gas embolism is an underrepresented medical condition, with high mortality rates (at times >46%[3]). While gas embolism occurs in several occupational circumstances,[13, 14] essentially any medical procedure can lead to it, like laparoscopy,[15] peripheral venous

catheterizations,[16-19] hysteroscopic endometrial ablation,[3-5, 20-23] cardiopulmonary resuscitation,[24] or during wound irrigation with disinfectants like hydrogen peroxide.[25]

Furthermore, gas embolism can be the consequence of abrupt changes in pressure experienced by the body, for example, deep-sea scuba diving, high altitude flying, aerospace operations[26] or even during explosions and aggression-induced traumas.[27-30] Occupational divers encounter significant breathing hazards and mortality issues such as decompression sickness, C.G.E., compression pains, barotrauma, oxygen toxicity, hypoxia, and breathing gas contamination, like carbon monoxide.[31] It is estimated [32] that at least 70% of occupational sea divers experienced decompression sickness and that this incidence is even higher in low-income and middle-income countries. Furthermore, decompression sickness is presently an underestimated professional hazard for aquaculturists and deep-sea divers, [33] as climate change forces deeper diving.[34]

Presently, the morbidity and mortality of gas embolism cannot be completely quantified due to the complexity of reported cases, possibly coupled with underreporting. However, based on retrospective studies, it was established that gas embolism is one of the major critical issues in intensive care units (I.C.U.s).[35-37] Gas embolism can be a common unintended outcome during surgery, such as neurosurgery, coelioscopy, endoscopy, hemodialysis and central venous catheterization.[38, 39] Furthermore, the advancement of new surgical techniques, such as invasive vascular approaches and probing of tissues during surgeries, is likely to have an impact on the increase of incidence in gas embolism events. [26]

While the events following gas embolism complications were relatively well-reported,[7, 16, 40-42], the physical triggers of gas embolism *genesis* and the events before a pathological condition is apparent, are still ambiguously and poorly described.[43] Consequently, a fundamental understanding of the relationships between gas emboli environmental parameters and their evolution can provide an important framework for treating gas embolism. Fortunately, microfluidics technology offers a convenient and versatile tool to explore the relationships between liquid and air parameters related to gas embolism.[44-47] Recent works reported microfluidics for *in vitro* characterization of bubble dynamics which was further verified by *in vivo* investigations.[48] More generally, the capability of the ever-advancing microfluidic systems to study complex physiochemical and biological phenomena in live tissues was repeatedly and frequently demonstrated.[49-53]

Poly-dimethyl-di-siloxane (PDMS) is a material frequently used for microfluidic device fabrication[54], including studies related to gas embolism.[48, 55, 56] PDMS is an elastomeric polymer with well-established microfabrication protocols[57] and many beneficial properties, like optical transparency, which is essential for microscopy studies,[58-55] high replication precision by soft lithography,[54] and biological compatibility for cell studies.[53-55] Additionally, PDMS presents mechanical and physio-chemical properties, e.g., high oxygen diffusivity, high elasticity, surface wettability, that can be modulated by exposure to U.V. radiation or oxygen plasma, making it a strong candidate for mimicking vascular tissues.[59, 60] For instance, the Young modulus of PDMS ranges from 0.05 to 2 MPa,[60] and up to 5 MPa,[61] compared with 0.04 to 2 MPa for human abdominal aorta sections, and 0.05 to 1.45 MPa for the human iliac artery,[62] and in cerebral arteries up to 5 MPa.[63] Furthermore, while the normal O_2 diffusivity of PDMS is higher than that of blood vessels, namely, 3.4×10^{-5} cm^2/s,[64, 65] compared with $\sim 10^{-6}$ cm^2/s,[66] both mechanical and physicochemical properties of PDMS are tunable by polymer-crosslinker composition and curing conditions.[57, 59, 67]

A previous study[56] investigated the dynamics of red blood cells (local cell concentration) and other cell-free components (cell-free layer) of the blood around gas bubbles in linear channels. This study used blood-like dextran 40 containing 10% of bovine red blood cells (RBC.s) in microfluidic channels to demonstrate the concentration of cells was higher upstream of the bubble than downstream. Subsequent work[55] studied the displacement of exogenously introduced bubbles and their size evolution in two

different hematocrit concentrations (5% and 10%), by using a multilevel bifurcations microfluidic device which led to an asymmetric division of the air bubbles. Recently, a *in vitro* microfluidics-based investigation provided an explanation of the environment around the gas emboli and the clot formation based on the flow-field hypothesis.[48] This study investigated the formation of Taylor-bubbles (elongated bubbles in channels) using a glycerol-based liquid medium in a serpentine channel with T-junctions. The blood clot formation process and the impact of coagulation on bubble movement were explained based on Taylor-Bretherton's theory and Laplace's theory, and described how the localized thrombus formation upstream severely reduces the flow velocity (Taylor-Bretherton's theory) due to thrombus induced resistance and thus halts the bubble displacement (Laplace's theory) due to clotting.[48]

Despite the numerous clinical works concentrating on mitigating surgery-derived or occupationally-derived pathological effects of gas embolism,[26, 41, 68-70] only a few studies focused on mimicking gas embolism in microfluidic systems.[48, 55, 56, 71, 72] However, most of these studies focused on embolism in large blood vessels, e.g., 100 μm, or used blood flow rates or air pressures that are less biologically relevant. Also, many more questions regarding the impact of real-life parameters on gas embolism genesis are waiting for answers, such as: What is the effect of micro-vessel diameter (if less than 100 μm) on the genesis of gas embolism? Is there a particular angle of air entry that aggravates the risk of gas embolism? Can bifurcation angles impact emboli displacement? How does blood viscosity affect vessel blockage? Based on viscosity, are there individuals with a higher risk of experiencing a gas embolism event?

To answer these questions, the present work studied previously unexplored diameter ranges of microfluidic structures mimicking blood vessels (namely 20 μm, 30 μm, 40 μm and 60 μm), using three different biologically relevant hematocrit concentrations including 0%, 20%, and 46%, for reference, anemic, and normal hematocrit concentrations, respectively. Different liquid-to-air ratios, like 1:10 to 1:100, were assessed in linear channels with T- and Y-junctions, as well as in complex, arterial bifurcation-like channels.

2. Materials and methods

2.1. Microfluidic chips and overall experimental setup

The experimental setup is presented in **Fig. 1A**, and various geometries of the channels mimicking microvasculature are presented in **Fig. 1B** and **Fig. 1C**. These designs consisted of linear channels with two configurations, namely, T- and Y-junctions, and a network of channels with 30 μm widths connected in honeycomb-like patterns with three bifurcation angles, namely, 30°, 60°, and 90° (**Fig. 1B** and **Fig. 1C**). The linear channels with T- and Y-junction entries with widths of 20 μm, 40 μm, and 60 μm were used to investigate the effect of the liquid-to-air mixing interface, the liquid slug, and the properties of air bubbles (**Fig. 1A**, bottom). The honeycomb-shaped network, comprising six bifurcation levels with 30 μm width was used to assess the impact of the bifurcation angle on the displacement of bubbles. More details of the channel architecture are presented in the Supplementary Information **Fig. S1**.
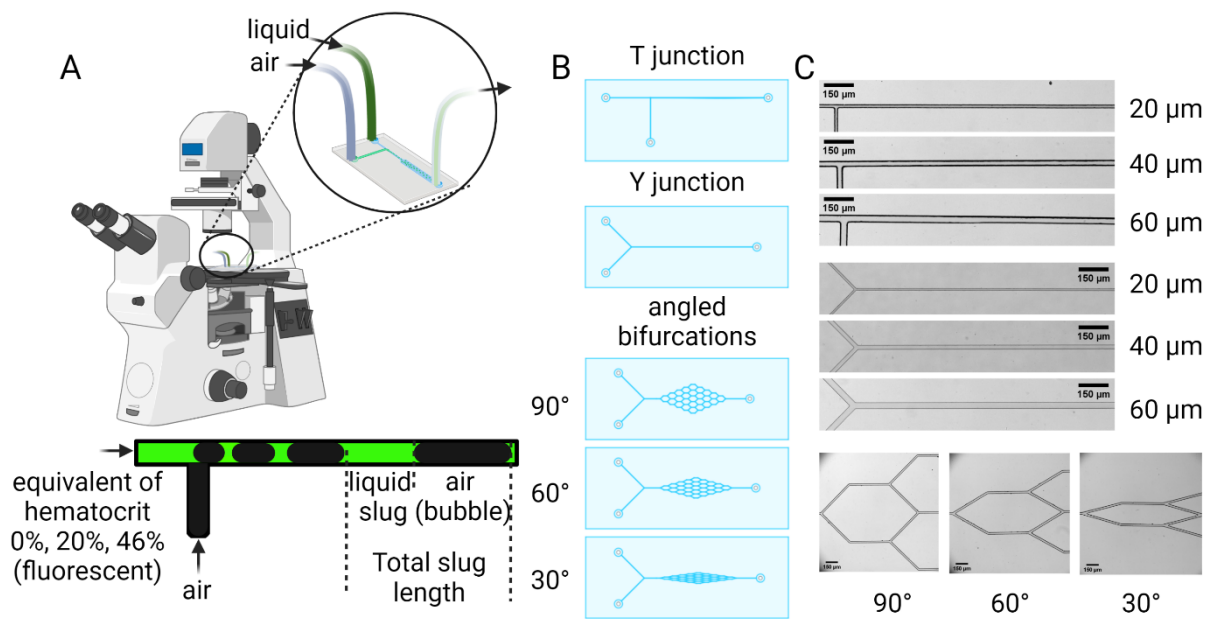
Figure 1. Experimental setup and microvascular-mimicking architectures used for the study of gas embolism. **A.** The experimental setup includes a microscope (Olympus IX83) and the microfluidic device (in the inset) with inlets for air (in blue) and fluorescent liquid (in green), outlet (in light green). The inlets are connected to programmable syringe pumps. The schematics showing the inlets, the fluid viscosities used in this study, the sizes of air bubbles, liquid slugs and total slug units and their boundaries are presented in the lower part of **A**. The overall designs (**B**.) and optical images (**C.,** partial) of the microvasculature structures used for studying the parameters that modulating gas embolism *in vitro*.

Standard SU-8 photolithography technique was used to fabricate the silicon master wafers, followed by PDMS soft lithography replication. The devices were treated with oxygen plasma and sealed on clean glass slides. The fabrication procedure is illustrated in Supplementary Information **Fig. S2**. The experimental setup used programmable syringe pumps (Pump 11 Elite Syringe Pumps, Harvard Apparatus) to inject different working fluids into the microfluidic chips. An inverted confocal microscope (Olympus IX83 fluorescence microscope, Olympus Corporation) with a high–speed camera was used for visualization. All experiments were carried out using a Uplano 4X magnifying objective for linear channels, and a UPlano 1.25X magnifying objectives for the bifurcated complex networks, which provided a larger field of view. The images were acquired at the mid-plane of the microfluidic chips at a frame rate of 100 frames per second (fps) by a high–speed camera (C11440-42U30, Hamamatsu Photonics K.K.).

2.2. Working fluids

The three working fluids used in this study vary in viscosity which is tailored to match the rheological properties of blood at 20%, and 46% hematocrit concentrations, and using water as benchmark fluid which is equivalent to 0% hematocrit. The preparation procedure was adopted from other study.[73] The synthetic hematocrit formulation consisted of 60% water, 40% glycerin, and a varying total amount of xanthan gum to mimic blood viscosities and rheological properties (0.0075% and 0.04% for equivalent concentrations of 20% and 46% hematocrit, respectively). The liquid flow rates were selected based on blood flow in human arterioles.[74] For the channels with widths of 20 µm, 30 µm, 40 µm, and 60 µm, the liquid flow rates were 12 µl h^{-1}, 24 µl h^{-1}, 42 µl h^{-1}, and 90 µl h^{-1}, respectively. For fast high-quality imaging, fluorescein, a green, fluorescent compound was mixed with the working fluid (1 ml of 2% stock solution for 50 ml working fluid) to track the movement of the liquid slugs and liquid phase in conjunction with the gas bubbles and the gas phase flow.

2.3. Image analysis

The acquired images were processed by ImageJ FIJI software to measure the size and velocity of liquid slugs and air bubbles. The data analysis was performed using MATLAB codes specifically developed to identify liquid slugs and air bubbles based on fluorescence intensity using 8-bit microscopy images converted to binary images. Image analysis and image type conversion were based on protocols reported elsewhere.[75] GraphPad and MATLAB-based graph plotting tools were used to plot the datasets.

3. Results and discussion

Slug flow (or Taylor flow) is defined as the successive displacement of a total slug unit composed of an air bubble and a liquid phase known as liquid slug.[76] The **Movie SI 1** (Supplementary Information) presents the typical results from microscopy in the experiments. The green fluorescence represents the liquid interface, while zero-fluorescent channels represent the gas bubbles. The experimental parameters, namely, equivalent concentration of hematocrit, channel width, junction type, and the liquid-to-air ratio, influenced the observed flow patterns (**Section 3.1**) and physical properties of total slug behavior (**Section 3.2**) in different experimental conditions as detailed below. In this study, the length and velocity of air bubbles and liquid slugs were used to quantitatively interpret the impact of the experimental parameters.

3.1. Flow patterns of liquid slugs

In general, the various geometries of the microfluidic systems, including channel widths, T- or Y- junctions (**Fig. 1B** and **Fig. 1C**), coupled with the fluid properties, namely liquid-to-air ratios and equivalent concentrations of hematocrit, resulted in four typical flow patterns (**Fig. 2A-E**, and **Mov. SI1**). **Fig. S3** presents a more detailed panoply of the flow patterns obtained for all experimental conditions used in this work. These flow patterns are briefly described as follows:
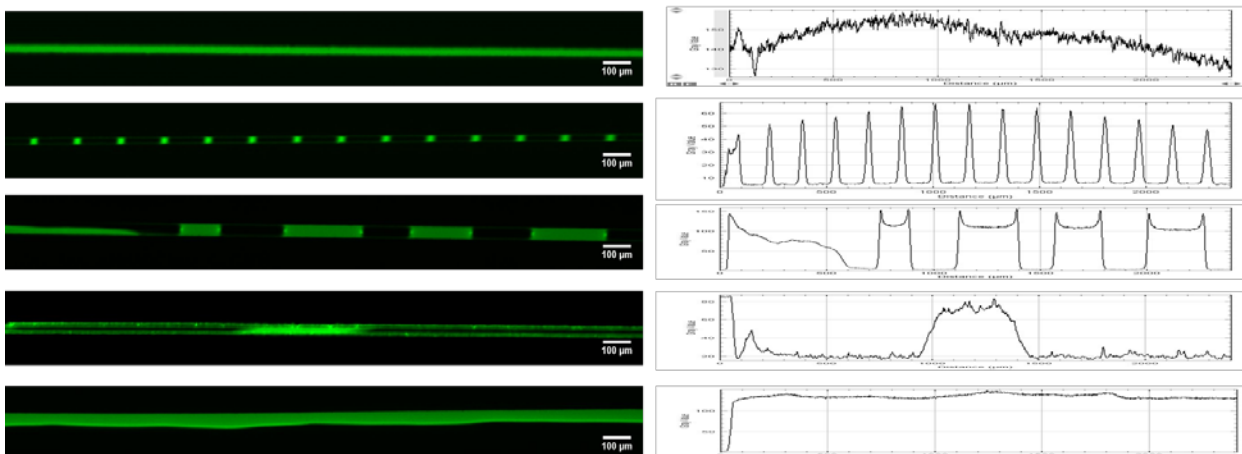
Figure 2. Flow patterns in different microfluidic structures mimicking blood vessels. **A.** Continuous flow (single liquid phase flow). **B.** and **C**. Liquid dominated pattern, repetitive air bubbles in liquid slug flow, with different dimensions and frequencies. **D**. Air-dominated pattern, liquid in air bubble flow. **E**. Stratified behavior, continuous laminar flow. Slug flow patterns were observed in B, C and D. The intensity plot profile compares the intensity of fluorescence spikes due to liquid slug flow in the channels.

Continuous flow of a single liquid phase. The continuous flow pattern was predominant at low liquid-to-air ratios, especially below 1:10, at the highest equivalent concentrations of hematocrit, namely, 20% and 46%, and larger channel widths. For these conditions no air bubbles were formed in the fluid flow (**Fig. 2A**). The presence of T-junctions translated in a higher propensity for continuous flow of a single liquid phase than the Y-junctions.

i. *Liquid-dominated, recurrent alternating air-in-liquid slug flow.* This pattern appeared as air locked in a liquid-dominated flow. Higher equivalent concentrations of hematocrit, and most cases of flow rates in channels with Y-junctions, translated in this flow pattern. However, two variants were observed, that is regular, short liquid slugs with long air bubbles (**Fig. 2B**) and irregular long liquid slugs with long air bubbles (**Fig. 2C**). **Fig. 2B** and **Fig. 2C** present this flow pattern for Y-junctions, also observed in T-junctions with larger channel widths namely, 60 μm (**Fig. S3**).

ii. *Air dominated, recurrent liquid-in-air bubble flow.* This pattern (**Fig. 2D**) occurred predominantly for liquids with lower viscosities, and in networks with T-junctions (regardless of the channel width) at liquid-to-air ratios above 1:40 for water and above 1:80 for 20 and 46% equivalent concentrations of hematocrit. In the tested conditions, this pattern was frequently observed with water in 20 μm channels and sometimes in 40 μm channels, with liquid-to-air ratios below 1:40. Lastly, the size of the liquid slugs was small compared to the length of the air bubbles.

iii. *Stratified, continuous laminar flow.* This type of flow pattern (**Fig. 2E**) was specifically observed in the channels with Y-junctions, for fluids with high viscosity, and at both low and high flowrate ratios (**Fig. S3**). The flow patterns of the alternating liquid slug and air bubbles transitioned to a flow with laminar and stratified aspect, where both the liquid and air flowed seamlessly as a continuous two-phase parallel flow. Finally, with high liquid-to-air ratios (higher than 1:80), the cross-section of the channel occupied by liquid, decreased.

3.2. Effective parameters of the gas bubble and liquid slug displacement in T- and Y-junction linear channels

Figs. 3 and **4** show the detailed flow patterns and the general liquid slug behavior in linear channels. **Figs. 3A** and **4A** are representative microscopy images and flow patterns of two liquid-to-air ratios for three equivalent concentrations of hematocrit and three channel widths with T- and Y-junctions (**Fig. 3** and **Fig. 4**, respectively). The microscopy image panel for varying flow patterns for all tested ratios and parameters, representing the air bubble size versus the liquid-to-air ratio ranging from 1:10 to 1:100, are provided in detail in Supplementary Information **Fig. S3**.

Fig. 3B-3C and **Fig. 4B-4C** present the size of air bubbles and liquid slugs versus the liquid-to-air ratio ranging from 1:10 to 1:100. In **Figs. 3B – 4B** and **Figs. 3C-4C,** the linear fit lines represent the trend in the sizes of air bubbles and liquid slugs observed across different flow ratios measured from several experiments (n ≥ 30 different measurements). The standard deviation (S.D.) represented the length variations of the air bubbles and liquid slugs at a particular liquid-to-air ratio. High differences resulted from the fluctuating air pressures and reduced liquid slug displacement in the channels during the onset of emboli. Conversely, smaller variations of air bubbles and liquid slug sizes corresponded to uniform, reproducible flow patterns and predictable sizes of total slug units. Three parameters, namely (i) channel width; (ii) equivalent concentration of hematocrit, and (iii) liquid-to-air ratios, in networks with T- and Y-junctions, influenced the uniform or non-uniform, fluctuating air bubble:liquid slug behaviors, further detailed below (**Figs. 3B** and **4B**).
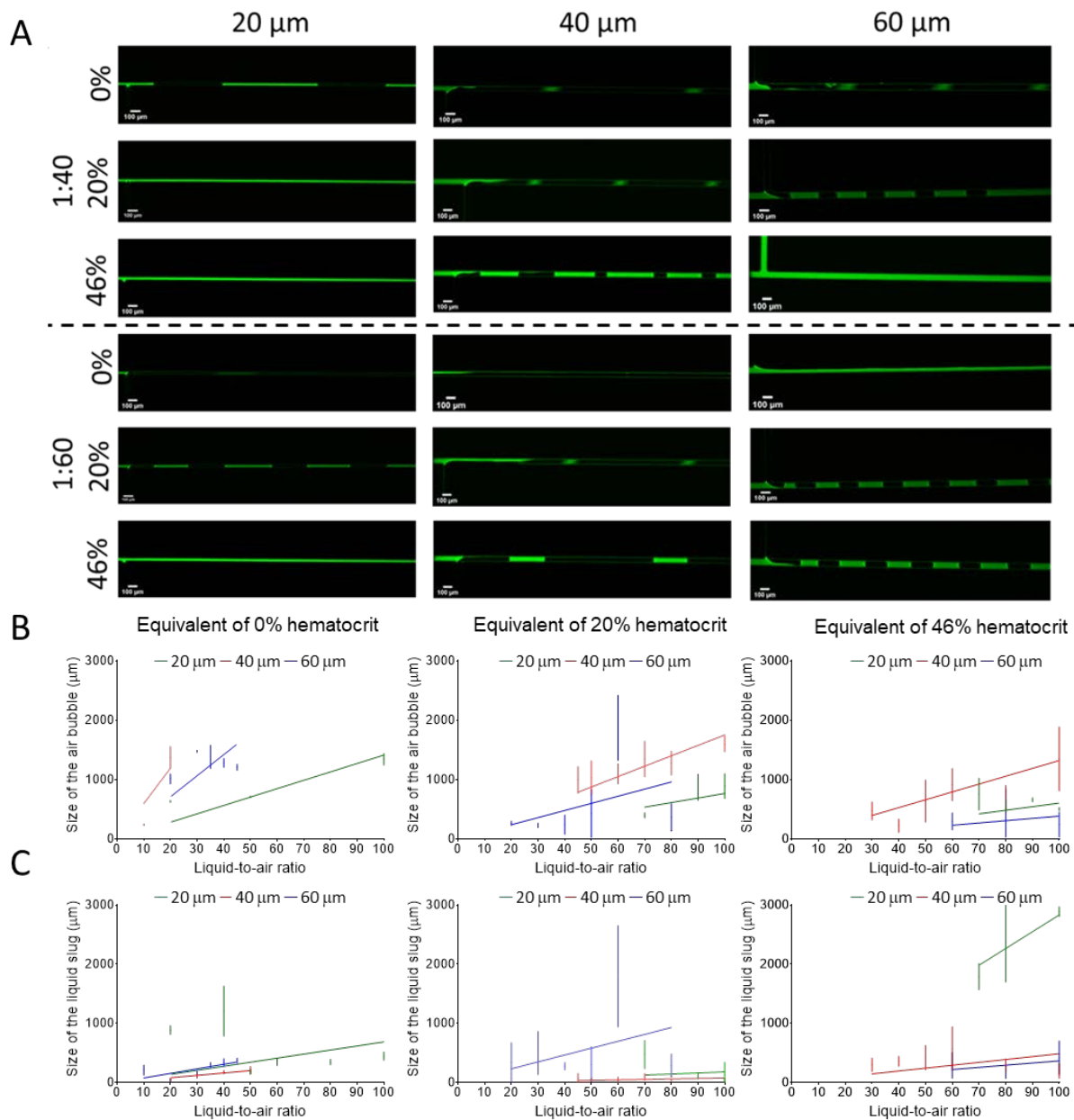
Figure 3. Flow patterns in linear channels with T-junctions, for different liquid-to-air ratios. **A.** Fluorescent micrographs of the representative flow patterns for different channel widths, viscosities, and liquid-to-air ratios. The full description of flow patterns is presented in Supplementary Information. **B.** Graphs of the measured the sizes of air bubbles and liquid slugs across different liquid-to-air ratios. The standard deviation (S.D.) represents the size variation of the air bubbles and liquid slugs calculated from the observed values in linear channels. The larger S.D. represents larger fluctuations in the size of air bubbles and liquid slugs. The three graphs represent three different viscosities.

3.2.1. Channels with T-junctions

Effect of equivalent concentrations of hematocrit. The different equivalent concentrations of hematocrit used in this study impacted the flow patterns in the channels. As the viscosity of the injected liquid increased, the size of the air bubble decreased, irrespective of the channel width (**Fig. 3B**). Viscosity-derived reduction in the size of air bubbles was observed during the injection of liquids with an equivalent concentration of 0% hematocrit. An example of this occurrence is presented in **Fig. 3B**. The slight increase in liquid-to-air flow ratios, i.e., above 1:20, led to a rapid increase in bubble length, i.e., longer than 1500 µm, typically beyond the field of view of the microscope objective. Working

fluids with 0% and 20%, equivalent concentrations of hematocrit showed a dependence of the channel width on bubble size (larger to smaller) 40 μm, 60 μm and 20 μm (red, blue, and green lines, respectively in **Fig. 3B**). Also, the difference between sizes of air bubbles for different widths was considerable. However, for the equivalent concentration of 46% hematocrit, the sizes of air bubbles started to decrease, and the significant differences presented before due to channel widths dwindled, as clearly observed in **Fig. 3C**. It is also notable that the size of air bubbles decreased and the average trendlines were not significantly different anymore for larger width channels (green - 20 μm, red - 40 μm, and blue - 60 μm lines (**Fig. 3B** and **3C**)). The variability in the sizes of air bubbles and liquid slugs was represented as the standard deviation (S.D.), vertical lines in the graph (**Fig. 3B**, **4B** and **5**). Longer vertical lines for S.D represent higher fluctuations in the measured sizes of the air bubbles and the liquid slugs, and shorter vertical lines indicated lower fluctuations or reproducible bubble sizes and liquid slug sizes. Higher fluctuations were significant for liquid-to-air ratios between 1:60 to 1:80 across the equivalent concentrations of 20% and 46% hematocrit, while the S.D slightly varied (shorter vertical lengths) for the equivalent concentration of 0% hematocrit. Overall, an increase in the liquid viscosity led to a higher fluctuation in the sizes of air bubbles and liquid slugs at moderate liquid-to-air ratios (1:40 to 1:80). This can be explained based on the Newtonian fluid behaviour of water, leading to a smaller variability (S.D.) trend. However, the non-Newtonian fluid behaviour of the two different equivalent concentrations of hematocrit showed higher fluctuations in the size of air bubbles.

Effect of channel width. Three different widths in linear channels were tested, i.e., 20 μm, 40 μm, and 60 μm. The size of the air bubble varied non-linearly with the widths of the channel, with a maximum air bubble size for the 40 μm channel, irrespective of the equivalent hematocrit concentration. At higher liquid-to-air ratios, the size of air bubbles was larger than the field of view of the microscope objective. Irrespective of the channel widths and liquid-to-air ratios, the lengths of liquid slugs were below 1000 μm, as presented in **Fig. 3C**, with the notable exception of the narrowest channel (20 μm) and the highest viscosity (46% equivalent concentration of hematocrit). Indeed, working fluids with higher viscosities flowing in narrow channels induced a higher liquid-to-air resistance and, thus, promoted the creation of larger liquid slugs.

Effect of liquid-to-air ratios. The size of air bubbles increased with increasing liquid-to-air ratios. As a qualification, the viscosity reduced this relationship. On the other hand, the variation of the size of liquid slugs was quite unpredictable and no obvious trend was observed. In some cases, the liquid-to-air ratio was too low to physically mimic gas embolism. In such instances, a continuous single liquid phase was observed (**Fig. 2A**). This flow pattern was representative for the 20 μm channels and a working fluid with an equivalent concentration of 46% hematocrit. When increasing the liquid-to-air ratios, the preponderance of air bubbles, in terms of occupancy per unit area in the channel, increased. An increase in the liquid-to-air ratio translated into a shift in the flow regime from liquid-dominated, i.e., "air in liquid" pattern (**Fig. 2B** and **C**), to air-dominated, that is "liquid in air" pattern (**Fig. 2D**). The translation in the flow regime led to a decrease in the sizes of the liquid slugs, and conversely, the size of air bubbles increased. This effect was predominantly observed for liquid-to-air ratios higher than 1:60 with fluids with low equivalent concentrations of hematocrit (0% or 20%). Higher flow rates and a high equivalent concentration of hematocrit (i.e., 46%) translated into a stratified flow pattern in larger microchannels like 60 μm (**Fig. 2E**). Finally, the size and frequency of liquid slugs increased across different widths with increasing liquid viscosities.

3.2.2. Channels with Y-junctions

Effect of equivalent concentrations of hematocrit. Similar to the effect of viscosity on the size of air bubbles in channels with T-junctions, as the viscosity increased, the size of air bubbles decreased, irrespective of the channel width. In the 20 μm channels, the effect of an increase in the liquid viscosity led to short liquid slugs and air bubbles (**Fig. 4A** and

Supplementary Information **Fig. S3**). Also, similar to the channels with T-junctions, for flow with fluids at an equivalent concentration of 0% hematocrit, and with a low liquid-to-air ratio (1:20), the bubble size rapidly increased beyond the field of view. For the equivalent concentrations of 0% and 20% hematocrit, the order of width-dependent (green - 20 μm, red - 40 μm, and blue - 60 μm lines **Fig. 4B** and **4C**) air bubble size was similar. However, at the equivalent concentration of 46% hematocrit, the size of air bubbles started to decrease, and the differences observed between the different widths decreased too. Viscosity played a similar role on air bubble sizes and liquid slugs as for the experiments using channels with T-junctions, with some notable exceptions, as detailed below.
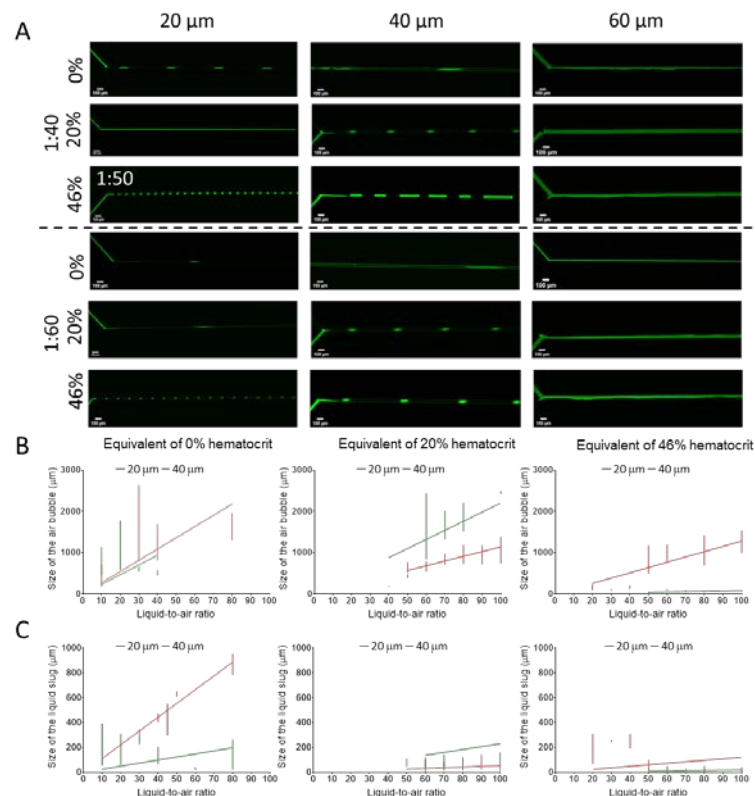
Figure 4. Flow patterns in Y-junction linear channels for different liquid-to-air ratios. **A.** Fluorescent micrographs of the representative flow patterns for different channel widths, viscosities, and liquid-to-air ratios. The full description of flow patterns is provided in Supplementary Information. (**Fig. S3**) **B.** Graphs of the measured the sizes of air bubbles and liquid slugs across different liquid-to-air ratios. The standard deviation (S.D.) represents the size variation of the air bubbles and liquid slugs calculated from the observed values in linear channels. The larger S.D. represents larger fluctuations in the size of air bubbles and liquid slugs. The three graphs represent three different viscosities.

Effect of channel width. An increase in the width of the channel decreased the frequency of the liquid slugs and air bubbles (**Fig. 4A**, horizontal comparison). Compared with larger widths, the 20 μm channels presented a higher frequency of liquid slug and air bubble alternating flow, for all fluid viscosities. As the width increased, the frequency decreased to the extent that for 60 μm channels, no liquid slug and air bubble alternating flow was observed. An increase in channel widths from 20 μm to 40 μm increased the air bubble size, but most 60 μm channels presented a stratified flow pattern. The alternating flow of liquid slugs and air bubbles was replaced by a streamlined, parallel flow of separate liquid and air phases, even for low liquid-to-air ratios. For the T-junction channels of the same width, streamlined, parallel flow was only observed at high liquid-to-air ratios (like 1:120, for the equivalent concentration of 0% hematocrit, **SI Fig. S3**). The flow of fluids with lower equivalent concentrations of hematocrit in narrow channels resulted in a transition from an "air in liquid" pattern to a "liquid in the air" pattern (**Fig. 2B** and **C**). This transition was typical for liquid-to-air ratios below 1:60 in both T- and Y-

junctions (**Fig. S3**). A lower frequency of alternation between liquid slugs and air bubbles was observed for 40 μm channels, compared to 20 μm. The 60 μm channel presented mostly stratified flow patterns (**Fig. 3A** and **4A**, **Fig. S3**).

Effect of liquid-to-air ratios. The size of air bubbles increased with increasing liquid-to-air ratios similar to the channels with T-junctions. However, an increase in the equivalent concentration of hematocrit dampened the rate of rising bubble sizes due to the increased resistance of air bubbles to liquid viscosity **(Fig. 4A-C)**. Unlike the channels with T-junctions **(Fig. 3A-3C)**, those with Y-junctions presented a uniform alternating flow of liquid slugs and air bubbles with lower S.D. variations in their sizes and an increase of the liquid slugs with increasing channel width **(Fig. 4A)**. Viscosity variation led to an increased frequency of liquid slug and air bubble alternating patterns**.** It was also observed that there was an intermittent release of bubbles into the liquid slug depending on the channel widths and liquid-to-air ratios. At lower liquid-to-air ratios, especially in the channels with smaller widths, e.g., 20 μm, a continuous liquid flow pattern was formed in which bubbles were released intermittently (**Fig. 2A**).

From the experiments detailed here, it can be inferred that the accumulation of pressure against the liquid interface, which will stop, or reduce the flow in channels, has a chaotic behaviour along with the unpredictable, non-uniform formation of air bubbles and their displacement. A higher equivalent concentration of hematocrit intensified this phenomenon, suggesting a higher likelihood of gas embolism in smaller vessels for patients with higher blood hematocrit concentrations like polycythemia,[77, 78] when the concentration can reach 50% or as high as 65% hematocrit. Moreover, the formation of longer air bubbles, or the intermittent discharge of air bubbles and liquid slug sizes, increases the possibility of microvasculature blockage.[71] This was confirmed when injecting high viscosity working fluids (equivalent concentration of 46% hematocrit) in 20 μm width channels. This observation was corroborated with velocity measurements, as described below. However, the intermittent release of air bubbles only slowed the velocity of the liquid slug, but it did not bring the flow to a halt or a blockage.

Previous studies used linear[55, 56] and serpentine channels[48] with larger widths for the study of gas embolism *in vitro*. The channel dimensions in the present study are lower than 100 μm, which is closer to the dimensions of arterial blood vessels. It is important to mention that previous work[48] reported that air bubbles stopped in the serpentine channels and inferred that this blockage is similar to gas embolism *in vivo*. However, in this study, and in the conditions reported here, exogenously generated bubbles, once injected in the network, continued until they reached the exit points for the total 3 cm length of the channels, without any detectable interruptions. One possible explanation is that serpentine channels present higher resistance than linear ones.[71] According to Laplace displacement in straight channels, the bubbles are displaced without any blockages, irrespective of the viscosity, and the reduction in viscosity is possible depending on multiple flow parameters like liquid-to-air ratio, surface wettability, and fluid properties while the same expectation may vary on serpentine channels.[48]

3.2.3. Velocity variation of the air bubbles and liquid slugs in T- and Y-junction channels

The velocity of liquid slugs in the channels with T- and Y-junctions, with different widths, and various liquid-to-air ratios are represented in **Fig. 5**. The velocity of air bubbles and liquid slugs are closely correlated, with no significant variations between them. Increasing the equivalent concentration of hematocrit led to a dampening velocity of the air bubbles. The resistance to flow with an increase in viscosity was observed more clearly for the 20 μm channels compared to those with 40 μm and 60 μm widths. As expected, the highest velocity was observed for the fluids with equivalent concentration of 0% hematocrit, while the highest dampening of velocity was observed for those with the equivalent concentration of 46% hematocrit. The velocity dampening trend with increasing viscosity was also observed in channels with Y-junctions. The stratified flow pattern in 60 μm channels did not show any individual air bubbles or liquid slugs. The

observation of the flow in movies showed that a decrease in the velocity of air bubbles increased the probability of bubble halting and therefore increased the chances of gas embolism events.
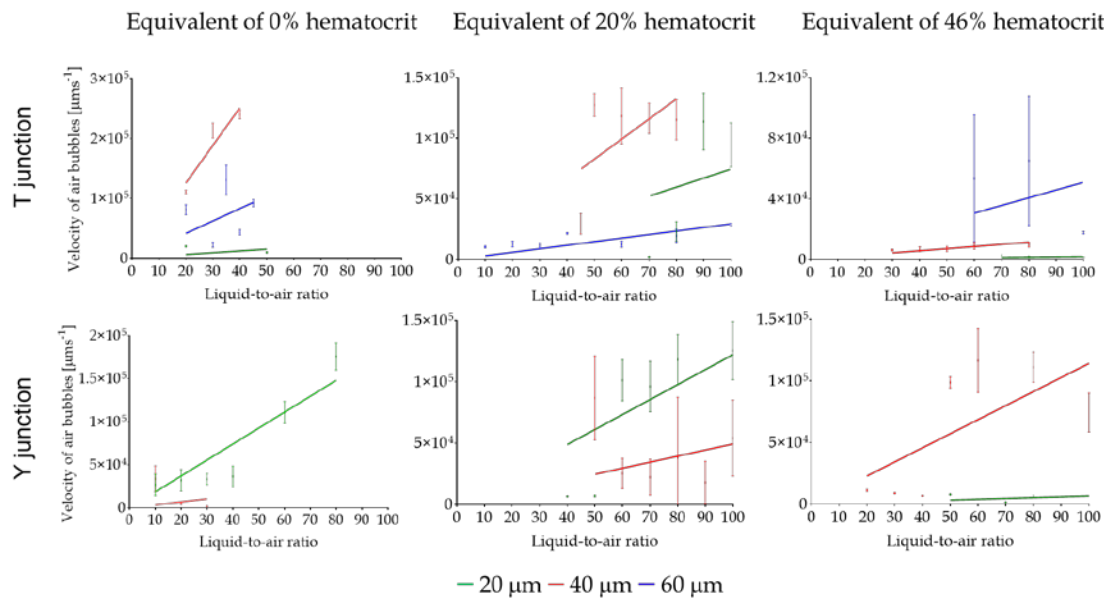
Figure 5. Effect of junction type, channel width, liquid-to-air ratio, and equivalent concentrations of hematocrit on the velocity of the liquid slugs. The standard deviation (S.D.) represents the velocity variation of the liquid slugs calculated from the observed values in the linear channels.

These velocity fluctuations of the fluid flow and bubble displacement, related to the channel width, viscosity, and the liquid-to-air flow rate, were evident by inspecting the variability (S.D.) of velocities (**Fig. 5**). A chaotic competition between liquid and gas interfacial forces can be a possible explanation for velocity fluctuation. The stable, uniformly alternating flow of liquid slugs and air bubbles decreased the variability in the velocity. However, the transition of fluid flow from the "air in liquid" pattern to "liquid in air" pattern (**Fig. 2**) promoted the variation of the sizes of liquid slugs and air bubbles.[44-47]

Overall, based on the analysis of the impact of junction types, it appeared that channels with 20 μm widths had higher chances for gas embolism events due to a non-uniform alternating behavior, frequent halting of the air bubbles, and higher resistance to flow of air bubbles. In channels with Y-junctions, an inverse relationship between channel width and velocity was observed, i.e., wider channels presented a decrease in velocity (**Fig. 5**, bottom row). However, there was no clear relationship between channel dimension and fluid velocity for channels with T- junctions. Similar to the velocity fluctuations observed in the 20 μm channels with T -junctions, those with 40 μm width and Y-junctions also had fluctuating velocities for all equivalent hematocrit concentrations.[44-47]

3.3. Complex honeycombed network of channels

Air resistance and gas embolism genesis were also studied in honeycombed structures with five generations of bifurcations. The honeycomb networks comprised Y-junction inlets and 30 μm width channels (**Fig. 1** and **Fig. S1**). A fluid with an equivalent concentration of 46% hematocrit was used. The key questions explored here were: Are there any angles that induce gas embolism events? How long are the air bubbles trapped in the bifurcations? And finally, can the air bubbles be washed or dissolved with high liquid-to-air ratios? The study with the complex bifurcation geometry was also used to

verify if Laplace displacement of bubbles occurred in more complex geometries with bifurcations at different angles as detailed below.

An ImageJ-based qualitative analysis of traffic density and dynamic regions of the honeycomb network results related to liquid slugs and gas bubbles is presented in **Fig. 6**. Additionally, the median bubble and liquid slug position in the nodes were used to quantitatively characterize the flow behavior of liquid slugs in complex bifurcated networks in **Fig. 7**.
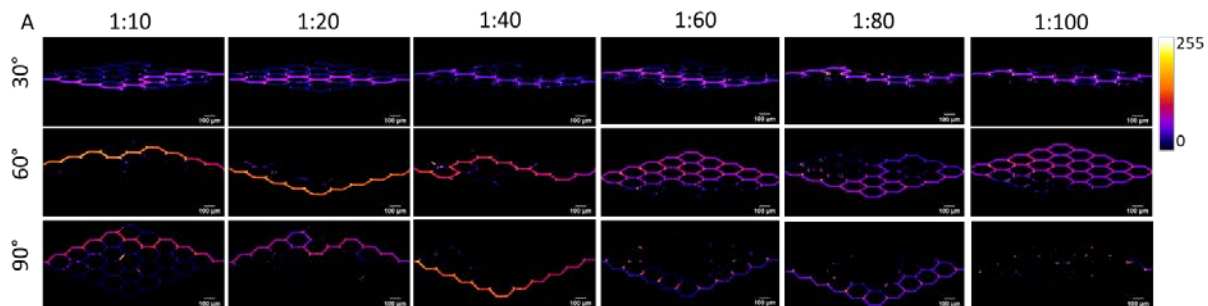
Figure 6. Total traffic density of the liquid slug, namely, bubble traffic in a complex bifurcation network for three different bifurcation angles. Higher intensities represent higher liquid slug to air bubble traffic. The dark channels represent blocked paths.

3.3.1. Mapping dynamic locations in the network

The density maps correspond to the dynamic routes in the bifurcation network where the air bubbles and liquid slugs are predominantly traversing, or where the traffic of liquid slugs and air bubbles was dense. The density maps were derived as total sums of the positions of air bubbles and liquid slugs in all the frames recorded for different flow ratios and equivalent concentrations of hematocrit. The dark regions showed blocked channels in the network while regions with varying intensities of blue to yellow show the flow of liquid slugs and air bubbles. Different bifurcation angles showed considerable differences in the total slug behavior. The bifurcation network showed three prominent flow patterns (**Fig. 7**): (i) flow in single channel, (ii) flow in partial networks, and (iii) flow in the entire network.

For example, flow of liquid slugs and air bubbles only in a single path (**Fig. 6**, first three columns) was observed for all the tested bifurcation angles, up to a liquid-to-air ratio of 1:40. For higher liquid-to-air ratios, the entire network had a different air bubble:liquid slug traffic, particularly for 60° bifurcation angles. For liquid-to-air ratios higher than 1:60 in honeycomb structures with 90° bifurcation angles no prominent patterns were observed. The density maps indicate that for 60° bifurcation angles there is an effective flow of air bubbles and liquid slugs, whereas for 90° bifurcation angles there is a higher risk for gas embolism events, especially at higher liquid-to-air ratios. In contrast, 30° bifurcation angles showed a selective flow pattern and an increased possibility for a gas embolism event to happen across the periphery channels.

3.3.2. Mapping stagnant features and blockages in the network

Mapping blockages and velocity fluctuations due to air bubbles was achieved through a median analysis, which is a static analysis demarcating the bubble trapping from continuous fluid flow. The dark or less-illuminated areas represent channels where continuous fluid flow did not occur due to blockages by gas bubbles. It is simply the average of the unchanging signals of either the air bubble (dark pixels) or the liquid slug (bright fluorescent pixels) from a stack of recorded microscopy images over several thousand frames. This analysis revealed the stagnant regions of the network and the regions where air bubble blockages were highly expected. Three types of network blockages were predominant: (i) blockages at the bifurcation junctions; (ii) blockages in

the channels; and (iii) blockages at both bifurcation junctions and in the channels (**Fig. 8A** and **8B**). The representative bifurcations with blocked bubbles and gas embolism events at different time points were shown in **Fig. 8**. It was observed that the stagnant points seldom moved over 50 seconds of the high-speed imaging performed here.
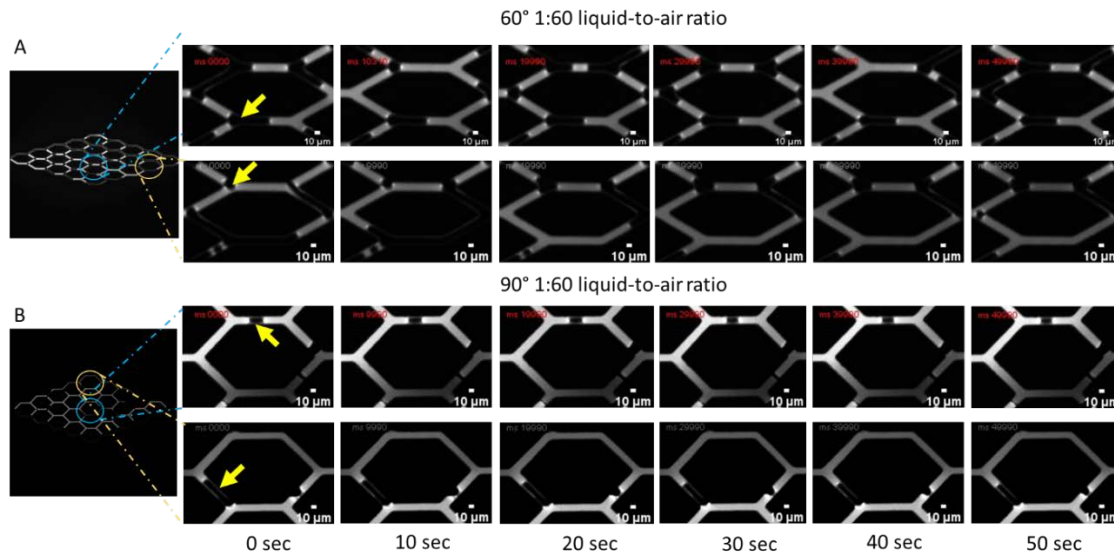
Figure 8. Time-resolved image analysis of the resilient bubbles. Median intensity plots of the blocked channels. The prevalence of gas bubbles and blockages at 1:60 flow ratios in 60° (A) and 90° (B) bifurcations. The bifurcation channels with 60° angles show gas emboli blocking at the junctions of the bifurcations, and 90° showing emboli in the channels. Yellow arrows indicate the position of the bubble stagnant over a period of time. The position of the bubble was predominant across each row of the images.

3.3.3. Velocity, retention time and size of air bubbles in the network

Apart from the qualitative image analysis provided by the density maps, a frame-by-frame quantitative analysis was made. The properties of air bubbles and liquid slugs, i.e., area, retention time in the network, and velocity, were measured. The respective graphs **Fig. 7B**, **7C**, and **7D**, were plotted from a minimum of 20 different track measurements across different conditions, like bifurcation angles and liquid-to-air ratios.

Velocity and retention time of air bubbles. Although velocity is dependent of the liquid-to-air ratio, a higher velocity of air bubbles means an unhindered flow of total slugs. Conversely, lower velocities indicated higher retention times, increased pausing, and possibly increased chances of the occurrence of a gas embolism event. Among the tested networks, only the 30° bifurcation network presented the lowest flow velocity (**Fig. 7B**) suggesting an increase in the retention time inside the channels. **Fig. 7D** shows that with a 30° bifurcation, the retention time did not decrease by increasing the liquid-to-air ratio, but rather increased the flow resistance and thus the possibility of a gas embolism event.

Size of air bubbles. An increase in the liquid-to-air ratio increased the sizes of air bubbles irrespective of the bifurcation angle since all the average bubble size data points overlapped within the S.D. variations (**Fig. 7C**). Thus, the bifurcation angle does not play a critical role in air bubble sizes.

Impact of liquid-to-air flowrate ratio on bifurcation angles. Comparing the fluid flow characteristics on the smallest bifurcation angles, i.e., 30°, and low liquid-to-air ratios, i.e., less than 1:60, the total slug followed a single path in the network rather than distributing throughout the geometry. Conversely, at higher flowrate ratios, namely above 1:80, the fluid flow dominated the entire network with a mixture of liquid slugs and varying sizes of air bubbles. With increasing angular bifurcations, e.g., 60°, the peripheral channels presented higher liquid slugs and air bubble flows (**Fig. 6** and **Fig. 7**). The median analysis also showed that two types of blockages in the junctions were expected depending on the

bifurcation angles. Overall, more acute angles of bifurcation presented an increasing probability of occurrence of gas embolism events.

Bubble flow patterns and liquid slug paths. By analyzing the images collected at 100 fps for over 1 minute, approx. 6000 frames, and inspecting the movement pattern of the air bubbles and liquid slugs in the network, the following conclusions were made:

1. The incoming bubbles from the inlets at any rate of liquid-to-air moved preferentially along the paths without bubble obstructions. As the air bubbles traversed the bifurcations and continuously entered the nodes without air bubbles, they eventually blocked all possible routes one after another, which led to blockage of partial regions in the network with no liquid flow (Supplementary Information, **Movie SI2**). This was observed across a large range of flow rates (1:10 to 1:100), for all bifurcation angles, but more often for 90° and 60° angles.

2. Lower generations of the bifurcations in the honeycomb showed frequent blockages (**Fig. 6** and **Fig. 7**). This is to be expected, as the air bubbles at the entry start to branch out, leading to air bubbles crowding in the second half of the network, thus leading to blockings across the lower half of the network with converging channels.

3. The phenomena mentioned in points (i) and (ii) led to selective blocking of many nodes, similar to tissue ischemia and regional systemic gas embolism. At moderate flow rates, between 1:20 to 1:60, the blocking effect was prominent for 30° and 60° angles. The 90° bifurcations presented the most air bubble trapping followed by 60° bifurcations, based on the median analysis of the recorded micrographs (**Fig. 7**). This variation in blocking appears to be a function of liquid-to-air ratios and bifurcation angles.

4. Monitoring the motion of air bubbles in honeycomb channels demonstrated that they move in the entirety of the network. The channels with air bubbles remained blocked for a while, until the pressure gradient of airflow increased sufficiently to displace them. This showed that the trapped bubbles, even if small, can block the flow in the downstream channels due to higher pressure drops compared with channels with only liquid slugs.
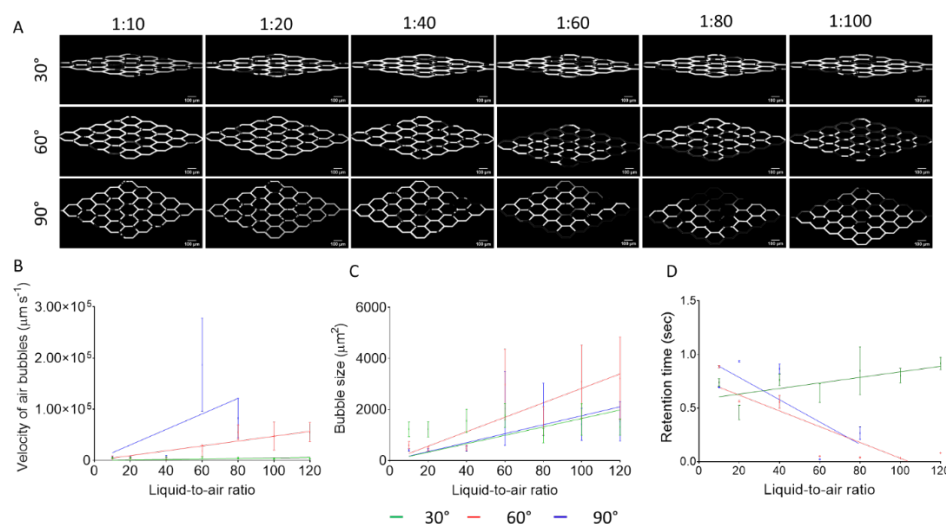
Figure 7. Median intensity plots of the blocked channels and traffic patterns for three differently angled bifurcations. The physical parameters namely, velocity of the air bubbles (A), bubble size (B), and retention time (C) in the network are shown in the graphs. The prevalence of gas bubbles and blockages at 1:40 flow ratios in 60° and 90° bifurcations are striking. The bifurcation channels with 60° angles show gas emboli blocking selective regions in the network. Bubble blocking the channels is shown as dark regions.

The architecture shown here is analogous to the branching of arterial vessels, which reaches the far end regions of the heart tissues.[79] Further work will focus on narrowing widths for angled bifurcations, commonly observed in arterial blood vessels from the heart to the extremities of the body tissue.[80]

3.4. Biomedical relevance of in vitro gas embolism

The environment surrounding air bubbles has been widely studied recently, particularly the cell-concentration upstream and downstream of the bubble and the contributing factors leading to gas embolism. Even if this study focused on the physical parameters of air bubbles and liquid slugs inside channels, there are a number of medically relevant findings that can be categorized as follows:

i. The arterial system presents blood vessels with decreasing diameters and a collective increase in cross-sectional area, which intensifies with further tapering down to capillaries while moving away from the heart. These channels are characterized by presenting the largest area and smallest diameters, narrowing towards the capillaries. This pattern is reversed for the venous system, with increasing diameters and decreasing cross sectional area. The pressure across the arterial system affects both positively and negatively the flow rates in the venous system and enables the diffusion of gases, nutrients, and metabolic products out of and into the blood. The focus of this work was on channels with smaller dimensions, i.e., less than 100 μm widths, to simulate the general arterial architecture, with working fluids of biologically relevant characteristics and flow rates.

ii. Many blood vessels bifurcate in a Y-junction pattern. Still, important T-junction exceptions occur, such as coronary arteries and Adamkiewicz's arteries, an important supply artery to the spinal cord, which takes a "hairpin turn".[81, 82] The central nervous system presents critical watershed areas with little collateral blood supplies. This study is relevant for this type of areas where the study of gas embolism is experimentally difficult and untenable due to its life-threatening aspect. Additionally, the possibility of laminar flow increases the chances of iatrogenic air injection into the vessels leading to rapid systemic embolism. The location of bubbles studied using the honeycombed device provided clues regarding the propensity of gas embolism in arterial-like bifurcation geometries**.**

iii. The impact of gas embolism may be influenced by blood viscosity,[46, 83] high or low blood pressures, obesity, lipid and cholesterol levels, and medications such as anticoagulants ("blood thinners" like warfarin and aspirin).[84] Hematocrit percentages vary largely among men and women by 42.4%±2.9% and 47.2%±2.4%, respectively.[85] It is generally lower than 42% for anemic individuals, although the percentages may be even lower depending on age and medical conditions. Furthermore, hematocrit concentrations can also vary between the upper and lower body by values of 40%±0.8% and 38.5%±0.8%, respectively. Thus, the three different working fluids studied here (equivalent of 0%, 20% and 46% hematocrit concentrations) are also relevant to biological conditions. For instance, the equivalent concentration of 20% hematocrit for low blood viscosity individuals under anticoagulants and blood thinners, an equivalent concentration of 46% for normal hematocrit concentrations present in humans,[86] and an equivalent concentration of 0% hematocrit when using analogous to water-type solutions used to irrigate internal organs when concluding a surgery. Additionally, blood components like albumin can contribute to cell-free blood which shares commonality with waterlike viscosity properties. Overall, the physical measurements of liquid slug behaviour presented here for different equivalent concentrations of hematocrit, including water as

reference liquid, can be related with iatrogenic or occupationally associated factors with higher risk of a gas embolism occurrence.

To recapitulate these findings and the results of previously published studies, **Table 1** summarises the *in vitro* studies performed in close relevance to gas embolism using a microfluidic setup mimicking blood vessel architecture.

Table 1. Relationship between the microfluidic chip design and fluid properties on gas embolism-relevant outcomes.

Chip design (width, µm)		Hematocrit concentration (%)	Liquid flowrate [µl h⁻¹]	Air pressure [mbar]	Gas embolism-relevant outcome	Medical relevance	Source
T-Junctions	20	Synthetic fluid equivalent to 0, 20 and 46% hematocrit	12	240-1440 µl h⁻¹ (1084 mBar*)	Smaller channels (20 µm) presented a higher air bubble resistance at higher equivalent concentrations of hematocrit. Wide fluctuations in the size of liquid slugs suggested an elevated risk of unpredictable gas embolism events.	Channel dimensions, viscosity, and liquid flow rates similar to the vascular system.	This Study
	40		42	252-5040 µl h⁻¹ (1084 mBar*)	The size and frequency of liquid slugs were stabilized with higher viscosities.		
	60		90	900-10800 µl h⁻¹ (1084 mBar*)	A stratified flow pattern was observed as a function of hematocrit concentration. Lower equivalent concentration of hematocrit increased the incidence of stratified flow.		
	100	5, 10	600	210 mBar	Local concentration of cells was affected by the passage of air bubbles.	RBC. mass transfer around the exogenous bubbles.	55
	350	10	240	25 mBar	Upstream of the bubble had high cell concentration. Spatial-temporal variations in cell-free layers and cell concentration due to the bubbles in the channels.	The genesis of clotting around the bubbles.	56
	600						
	100	-	-	200 to 800 mBar	A microfluidic study to understand the cellular response to bubbles in a microchannel.	Calcium response of endothelial cells to air bubbles.	72
	200	45*	1008*	100 mBar	Flow-field hypothesis and dynamics around the exogenous bubbles in the channels.	Study of coagulation events leading to the onset of embolism incidence.	48
Y-Junctions	20	Synthetic fluid equivalent to 0, 20 and 46% hematocrit	12	120-2400 µl h⁻¹ (1084 mBar*)	Viscosity increased the frequency of liquid slug and gas bubble alternating flow.	Y-junction is the least studied but most abundantly found junction in animals.	This Study
	40		42	420-6300 µl h⁻¹ (1084 mBar*)	The size of liquid slugs decreased with increasing viscosity. The size of liquid slugs became stabilized.		
	60		90	45-13500 µl h⁻¹ (1084 mBar*)	The stratified flow was common, irrespective of the channel width, viscosity, or liquid-to-air ratio.		
Honeycombs	30°	Synthetic fluid equivalent to 46% hematocrit	12	240-1440 µl h⁻¹ (1084 mBar)	A lower bifurcation angle (30°) presented a higher possibility of bubble trapping.	Bifurcation angle is critical for bubble displacement. Bifurcation angles are relevant to the likelihood of the occurrence of a gas embolism event.	This Study
	60°		42	240-1440 µl h⁻¹ (1084 mBar)	Presented the highest gas embolism occurrence.		
	90°		90	240-1440 µl h⁻¹ (1084 mBar)	The flows of liquid slugs and air bubbles were evenly distributed over the bifurcation network—a lower chance of gas embolism.		
	74°	5, 10	600	210 mBar	Asymmetric splitting of air bubbles leading to an uneven distribution of RBC.s in channels	Arterial type of bifurcated architecture.	55
	90°	45*	1008*	100	The monitoring of bubble displacement in the honeycomb shaped bifurcation geometry.	*In vitro* and *in vivo* models to study bubble displacement in bifurcation channels.	48

** This table summarises the studies performed in close relevance to gas embolism in blood vessels using a microfluidic setup.

*Calculated based on the reported data.

4. Conclusions

Air bubble dynamics and liquid slug flows depending on geometrical variations and operational parameters were monitored in both simple linear channels and complex honeycomb structures. Air bubble dynamics, such as size variation, indicated the competition between surface forces at the interphase of the liquid slug and the elongated air bubbles. The present work analysed smaller channel widths and liquid flowrates relevant to actual physiological conditions, as well as using fluids close to real blood viscosities derived from different hematocrit concentrations. Microvascular tissue-like structures using microfluidic networks with T- and Y-junctions and honeycombed networks were used due to their biological relevance. This study revealed important findings on the effect of viscosity, channel widths and equivalent concentrations of hematocrit on air bubble and liquid slug sizes and velocities to further simulate and understand gas embolism occurrences. Research on transport phenomena, gas embolism in microvasculature with smaller widths and more complex bifurcations with real blood and other conditions such as clot formation can become relevant subjects of future studies.

Authors' contributions: Mohammad Mahdi Mardanpour: conceptualization, methodology, validation, formal analysis, investigation, writing (original draft, review and editing), visualization. Ayyappasamy Sudalaiyadum Perumal: conceptualization, methodology, validation, formal analysis, investigation, writing (original draft, review and editing), visualization. Zahra Mahmoodi: data analysis, MATLAB coding for semi-automation of image analysis. Karine Baassiri: image analysis, writing (review and editing). Gala Montiel Rubies: image analysis, writing (review and editing). Kenneth M. LeDez: medical interpretation of results, writing (review and editing). Dan V. Nicolau: conceptualization, methodology, validation, formal analysis, review and editing of the original draft, visualization, supervision, project administration, funding acquisition.

Competing interests: Authors declare no competing interests. Data and materials availability: All data is available in the main text or supplementary materials.

Table of contents entry: The Investigation of gas embolism phenomenon, using a microfluidic system that mimicked the architecture of microvasculature.
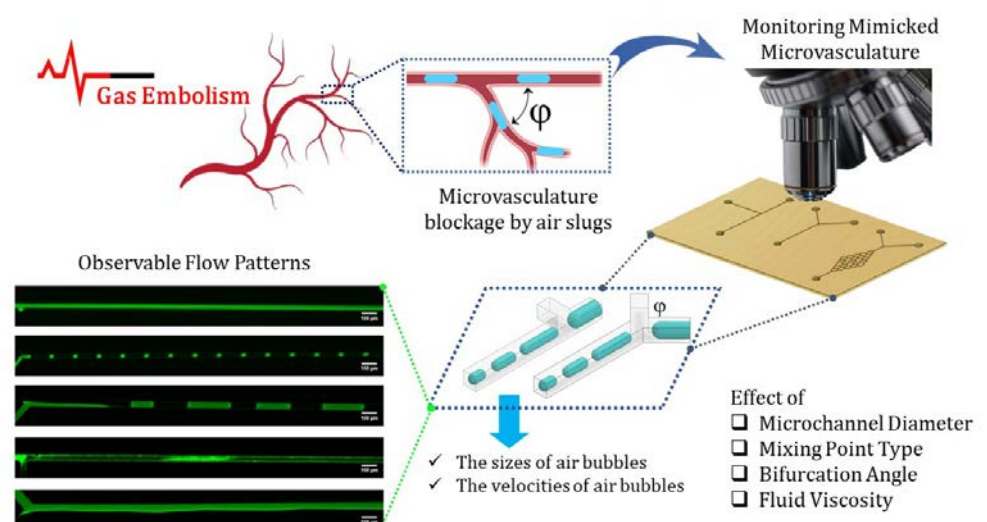
References

1. C. J. McCarthy, S. Behravesh, S. G. Naidu and R. Oklu, *Diagnostics*, 2017, **7**, 5.
2. M. A. Mirski, A. V. Lele, L. Fitzsimmons, T. J. Toung and D. C. Warltier, *The Journal of the American Society of Anesthesiologists*, 2007, **106**, 164-177.
3. S. Q. Liu, S. Z. Zhao, Z. W. Li, S. P. Lv, Y. Q. Liu and Y. Li, *Journal of Ultrasound in Medicine*, 2017, **36**, 749-756.
4. D. R. Stoloff, R. A. Isenberg and A. I. Brill, *The Journal of the American Association of Gynecologic Laparoscopists*, 2001, **8**, 181-192.
5. A. Verma and M. P. Singh, *Journal of Anaesthesiology, Clinical Pharmacology*, 2018, **34**, 103.
6. P. Mandelstam, C. Sugawa, S. E. Silvis, O. T. Nebel and G. Rogers, *Gastrointestinal endoscopy*, 1976, **23**, 16-19.
7. D. Hatling, A. Høgset, A. B. Guttormsen and B. Müller, *Acta Anaesthesiologica Scandinavica*, 2019, **63**, 154-160.
8. S. Mitchell and D. Gorman, *The Journal of extra-corporeal technology*, 2002, **34**, 18-23.
9. J. Pinho, J. M. Amorim, J. M. Araújo, H. Vilaça, M. Ribeiro, J. Pereira and C. Ferreira, *Journal of the neurological sciences*, 2016, **362**, 160-164.
10. M. ter Laan, E. Totte, R. A. van Hulst, K. van der Linde, W. van der Kamp and J.-P. E. Pierie, *European journal of gastroenterology & hepatology*, 2009, **21**, 833-835.
11. A. B. Branger and D. M. Eckmann, *Journal of Applied Physiology*, 1999, **87**, 1287-1295.
12. V. F. Tapson, in *Encyclopedia of Respiratory Medicine (Second Edition)*, ed. S. M. Janes, Academic Press, Oxford, 2022, DOI: https://doi.org/10.1016/B978-0-08-102723-3.00186-4, pp. 700-722.
13. I. Calder, *Occupational Medicine*, 1992, **42**, 213-214.
14. I. T. Parsons, E. D. Nicol, D. Holdsworth, N. Guettler, R. Rienks, C. H. Davos, M. Halle and G. Parati, *European journal of preventive cardiology*, 2021.
15. K. I. de Jong and P. W. de Leeuw, *European journal of internal medicine*, 2019, **60**, 9-12.
16. S. Allioui, S. Zaimi, S. Sninate and M. Abdellaoui, *Radiology Case Reports*, 2020, **15**, 1011-1013.
17. L. Dube, C. Soltner, S. Daenen, J. Lemariee, P. Asfar and P. Alquier, *Acta anaesthesiologica scandinavica*, 2004, **48**, 1208-1210.
18. O. Vignaux, P. Borrego, L. Macron, A. Cariou and Y. Claessens, *Undersea & Hyperbaric Medicine: Journal of the Undersea and Hyperbaric Medical Society, Inc*, 2005, **32**, 325-326.
19. C. Yang and B. Yang, *Neuroradiology*, 2005, **47**, 892-894.
20. P. Brandner, K. J. Neis and C. Ehmer, *The Journal of the American Association of Gynecologic Laparoscopists*, 1999, **6**, 421-428.
21. B. A. Dyrbye, L. E. Overdijk, P. J. van Kesteren, P. de Haan, R. K. Riezebos, E. A. Bakkum and B. M. Rademaker, *American journal of obstetrics and gynecology*, 2012, **207**, 271. e271-271. e276.
22. F. A. Groenman, L. W. Peters, B. M. Rademaker and E. A. Bakkum, *Journal of minimally invasive gynecology*, 2008, **15**, 241-247.
23. M. Paschopoulos, N. P. Polyzos, L. G. Lavasidis, T. Vrekoussis, N. Dalkalitsis and E. Paraskevaidis, *Annals of the New York Academy of Sciences*, 2006, **1092**, 229-234.
24. V. Arena and A. Capelli, *Cardiovascular Pathology*, 2010, **19**, e43-e44.
25. P. Zou, J.-S. Yang, X.-F. Wang, J.-M. Wei, H. Guo, B. Zhang, F. Zhang, L. Chu, D.-J. Hao and Y.-T. Zhao, *World neurosurgery*, 2020, **138**, 201-204.
26. T. S. Neuman, *Physiology*, 2002, **17**, 77-81.
27. A. M.-H. Ho and E. Ling, *The Journal of the American Society of Anesthesiologists*, 1999, **90**, 564-575.
28. C. Horrocks, *BMJ Military Health*, 2001, **147**, 28-40.
29. Y. Y. Phillips, *Annals of emergency medicine*, 1986, **15**, 1446-1450.
30. D. Riley, M. Clark and T. Wong, *Advanced Emergency Nursing Journal*, 2002, **24**, 47-59.
31. L. W. Raymond, *Journal*, 1998.
32. H. Bassett, 2019.
33. A. Boussuges, G. Chaumet, N. Vallée, J. J. Risso and J. M. Pontier, *Frontiers in physiology*, 2019, **10**, 749.
34. M. Barange, T. Bahri, M. C. Beveridge, K. L. Cochrane, S. Funge-Smith and F. Poulain, *United Nations' Food and Agriculture Organization*, 2018.
35. S. J. Brull and R. C. Prielipp, *Journal of critical care*, 2017, **42**, 255-263.
36. C. Ross, R. Kumar, M.-C. Pelland-Marcotte, S. Mehta, M. E. Kleinman, R. R. Thiagarajan, M. B. Ghbeis, C. J. VanderPluym, K. G. Friedman and D. Porras, *Chest*, 2021.
37. P.-M. Roy, A. Douillet and A. Penaloza, *Trends in Cardiovascular Medicine*, 2021.
38. J. Klein, T. A. Juratli, M. Weise and G. Schackert, *World neurosurgery*, 2018, **115**, 196-200.
39. T. Wu, Q. Wang, M. Zhao, Y. Zhu, L. Zhang, Y. Li and J. Li, *Journal of Forensic and Legal Medicine*, 2021, **82**, 102209.
40. A. M. Alexander and N. Martin, 2019.
41. B. Tufegdzic, M. Lamperti, A. Siyam and F. Roser, *Clinical Neurology and Neurosurgery*, 2021, **209**, 106904.
42. G. A. Vilos, J. R. Hutson, I. S. Singh, F. Giannakopoulos, B. A. Rafea and A. G. Vilos, *Journal of Minimally Invasive Gynecology*, 2020, **27**, 748-754.
43. S. Goldman, M. Solano-Altamirano and K. Ledez, *Gas Bubble Dynamics in the Human Body*, Academic Press, 2017.
44. D. M. Eckmann, J. Zhang, J. Lampe and P. S. Ayyaswamy, *Annals of the New York Academy of Sciences*, 2006, **1077**, 256-269.
45. D. Grulke, N. Marsh and B. Hills, *British journal of experimental pathology*, 1973, **54**, 684.
46. J. H. Kennedy, N. H. Hwang, S. G. Von Miller and A. Hartman, *Cryobiology*, 1974, **11**, 483-492.

47. J. L. Smith, D. H. Evans, P. R. Bell and A. R. Naylor, *Stroke*, 1998, **29**, 1133-1138.
48. Z. Li, G. Li, Y. Li, Y. Chen, J. Li and H. Chen, *Proceedings of the National Academy of Sciences*, 2021, **118**.
49. R. Abbasi, J. Liu, S. Suarasan and S. Wachsmann-Hogiu, *Lab on a Chip*, 2022, DOI: 10.1039/D1LC00905B.
50. L. F. Horowitz, A. D. Rodriguez, T. Ray and A. Folch, *Microsystems & Nanoengineering*, 2020, **6**, 1-27.
51. Z. Liu and X. Lan, *Lab on a Chip*, 2019, **19**, 2315-2339.
52. D. Marrero, F. Pujol-Vila, D. Vera, G. Gabriel, X. Illa, A. Elizalde-Torrent, M. Alvarez and R. Villa, *Biosensors and Bioelectronics*, 2021, **181**, 113156.
53. E. Moradi, S. Jalili-Firoozinezhad and M. Solati-Hashjin, *Acta biomaterialia*, 2020, **116**, 67-83.
54. K. Raj M and S. Chakraborty, *Journal of Applied Polymer Science*, 2020, **137**.
55. D. Bento, S. Lopes, I. Maia, R. Lima and J. M. Miranda, *Micromachines*, 2020, **11**, 344.
56. D. Bento, L. Sousa, T. Yaginuma, V. Garcia, R. Lima and J. M. Miranda, *Biomedical microdevices*, 2017, **19**, 1-10.
57. I. Wong and C. M. Ho, *Microfluidics and Nanofluidics*, 2009, **7**, 291-306.
58. M. Held, C. Edwards and D. V. Nicolau, *Fungal Biology*, 2011, **115**, 493-505.
59. K. Khanafer, A. Duprey, M. Schlicht and R. Berguer, *Biomedical Microdevices*, 2009, **11**, 503-508.
60. X. Q. Brown, K. Ookawa and J. Y. Wong, *Biomaterials*, 2005, **26**, 3123-3129.
61. R. N. Palchesko, L. Zhang, Y. Sun and A. W. Feinberg, *PLoS ONE*, 2012, **7**.
62. T. L. Poepping, H. N. Nikolov, M. L. Thorne and D. W. Holdsworth, *Ultrasound in Medicine & Biology*, 2004, **30**, 1067-1078.
63. K. L. Monson, W. Goldsmith, N. M. Barbaro and G. T. Manley, *Journal of Biomechanical Engineering*, 2003, **125**, 288-294.
64. T. C. Merkel, V. I. Bondar, K. Nagai, B. D. Freeman and I. Pinnau, *Journal of Polymer Science Part B: Polymer Physics*, 2000, **38**, 415-434.
65. M. Held, O. Kaspar, C. Edwards and D. V. Nicolau, *PROC. NATL. ACAD. SCI. U. S. A.*, 2019, **116**, 13543-13552.
66. A. Vadapalli, R. N. Pittman and A. S. Popel, *American Journal of Physiology-Heart and Circulatory Physiology*, 2000, **279**, H657-H671.
67. I. D. Johnston, D. K. McCluskey, C. K. L. Tan and M. C. Tracey, *Journal of Micromechanics and Microengineering*, 2014, **24**.
68. A. B. Branger, C. J. Lambertsen and D. M. Eckmann, *Journal of Applied Physiology*, 2001, **90**, 593-600.
69. R. Pearson, in *The physician's guide to diving medicine*, Springer, 1984, pp. 333-367.
70. R. A. van Hulst, J. Klein and B. Lachmann, *Clinical physiology and functional imaging*, 2003, **23**, 237-246.
71. T. Fu, Y. Ma and H. Z. Li, *AIChE Journal*, 2014, **60**, 1920-1929.
72. P. Ma, S. Wang, R. Guan, L. Hu, X. Wang, A. Ge, J. Zhu, W. Du and B.-F. Liu, *Talanta*, 2020, **208**, 120484.
73. K. Brookshier and J. Tarbell, *Biorheology*, 1993, **30**, 107-116.
74. T. E. Kornfield and E. A. Newman, *Eneuro*, 2015, **2**.
75. F. C. Van Delft, A. S. Perumal, A. van Langen-Suurling, C. De Boer, O. Kašpar, V. Tokárová, F. W. Dirne and D. V. Nicolau, *New Journal of Physics*, 2021, **23**, 085009.
76. J. Thaker and J. Banerjee, *International Journal of Multiphase Flow*, 2017, **91**, 63-75.
77. J. A. Garcia-Prats and L. E. Weisman, *UpToDate*, 2019.
78. A. Pappas and V. Delaney-Black, *Pediatric Clinics*, 2004, **51**, 1063-1086.
79. M. Zamir, *The Journal of general physiology*, 1988, **91**, 725-735.
80. Z. Li and G. H. Pollack, *bioRxiv*, 2021.
81. C. H. Alleyne, C. M. Cawley, G. G. Shengelaia and D. L. Barrow, *Neurosurgical Focus*, 1998, **5**, E2.
82. K. Yoshioka, H. Niinuma, S. Ehara, T. Nakajima, M. Nakamura and K. Kawazoe, *Radiographics*, 2006, **26**, S63-S73.
83. M. Akcaboy, B. Nazliel, T. Goktas, S. Kula, B. Celik and N. Buyan, *Journal of Pediatric Endocrinology and Metabolism*, 2018, **31**, 275-281.
84. C.-H. Lee, K.-H. Jung, D. J. Cho and S.-K. Jeong, *BMC neurology*, 2019, **19**, 1-7.
85. B. Y. S. Vázquez, *Vascular health and risk management*, 2012, **8**, 1.
86. H. H. Billett, *Clinical Methods: The History, Physical, and Laboratory Examinations. 3rd edition*, 1990.